SAND2014-20490C

Preliminary Field Test of the Wind Turbine Wake Imaging System

Thomas Herges[1], David Bossert[2], Randal Schmitt[3], David Maniaci[4], Crystal Glen[5], and Brian Naughton[6]
Sandia National Laboratories, Albuquerque, NM, 87185

The Sandia Wake Imaging System is being developed to improve the spatial and temporal resolution capabilities of velocity measurements within the inflow and wake of wind turbines for the purpose of validating high-fidelity models. Doppler Global Velocimetry has been selected for use by the Sandia Wake Imaging System for its ability to scale to large field of view while still capturing instantaneous coherent structures. A set of field tests have been conducted over a 2 m × 2 m viewing area to investigate how well the system could scale to larger viewing areas applicable to planned wind turbine field testing. Successful velocity measurements of a surrogate 1 m diameter fan flow were achieved which compared favorably to independent sonic anemometer measurements. The system sensitivity limits were analyzed over a range of signal levels to calibrate radiometric modeling used to scale the system for deployment at the Scaled Wind Farm Technology facility operated by Sandia National Laboratories through U.S. Department of Energy funding. Measurement results indicate the system was near the receiver shot noise limit and that an instantaneous velocity measurement with a 1 m/s noise is in all likelihood possible on a 5 m × 5 m viewing region at the Scaled Wind Farm Technology facility.

Nomenclature

Δf_b	=	frequency shift of frequency flat field
Δf_D	=	Doppler shift frequency
F	=	ICCD gain noise factor
G	=	camera gain
H_c	=	camera iodine cell intensity-to-frequency transfer function
H_p	=	phototube iodine cell intensity-to-frequency transfer function
I_r	=	reference camera intensity
I_s	=	signal camera intensity
$\hat{\boldsymbol{\imath}}$	=	incident unit vector
i_r	=	reference phototube integrated intensity
i_s	=	signal phototube integrated intensity
N	=	number of photons
$\hat{\boldsymbol{o}}$	=	observation unit vector
T_b	=	normalized frequency flat field camera intensity ratio
t_b	=	normalized frequency flat field phototube intensity ratio
T_D	=	normalized Doppler shift camera intensity ratio
t_D	=	normalized Doppler shift phototube intensity ratio

[1] Postdoctoral Appointee, Wind Energy Technologies Department, P.O. Box 5800.
[2] Principal Member of the Technical Staff, Optics and Sensor Engineering Department, P.O. Box 5800.
[3] Principal Member of the Technical Staff, Laser, Optics and Remote Sensing Department, P.O. Box 5800.
[4] Senior Member of the Technical Staff, Wind Energy Technologies Department, P.O. Box 5800.
[5] Senior Member of the Technical Staff, Contraband Detection Department, P.O. Box 5800.
[6] Senior Member of the Technical Staff, Wind Energy Technologies Department, P.O. Box 5800.
Sandia National Laboratories is a multi-program laboratory managed and operated by Sandia Corporation, a wholly owned subsidiary of Lockheed Martin Corporation, for the U.S. Department of Energy's National Nuclear Security Administration under contract DE-AC04-94AL85000.

V	=	flow velocity
v	=	velocity component along direction of velocity sensitivity
v_{neq}	=	noise equivalent velocity
α	=	angle between observation and incident laser unit vectors
Γ_b	=	frequency flat field intensity ratio of the cameras, I_s/I_r
γ_b	=	frequency flat field intensity ratio of the reference phototubes, i_s/i_r
Γ_D	=	Doppler shift intensity ratio of the cameras, I_s/I_r
γ_D	=	Doppler shift intensity ratio of the reference phototubes, i_s/i_r
Γ_f	=	intensity flat field ratio of the cameras, I_s/I_r
γ_f	=	intensity flat field ratio of the reference phototubes, i_s/i_r
η	=	photocathode quantum efficiency
λ	=	laser wavelength
σ_T	=	standard deviation of normalized Doppler shift intensity ratio

I. Introduction

A fundamental lack of understanding about the interaction between complex atmospheric flow structures and wind turbines still persists. As a result, current models fail to reliably predict wind farm performance, leading to uncertainty in optimizing wind farm design and layout [1-6]. Furthermore, the increased turbulence intensity produced within wind turbine wakes adds additional fatigue loading to downstream turbines, resulting in increased maintenance needs [7-9]. Experimental measurements of wind turbine inflow and wake at relevant spatial and temporal scales will improve understanding of the flow physics and provide validation for models used in the design of wind turbines and plants [10]. Numerous measurement technologies have been used to investigate the flowfields throughout wind farms and in the vicinity of wind turbines with varying temporal and spatial resolutions. The most promising non-intrusive velocity measurement technologies include scanning lidar [11-14], radar [4, 15, 16], and particle image velocimetry (PIV) [9, 17, 18]. Lidar and radar systems are extremely well suited for measuring average velocity and turbulence statistics over a large area near utility scale wind turbines and throughout wind farms. However, they are limited in their capability to offer instantaneous realization of coherent turbulent structures produced by wind turbines [4, 11]. Capturing of these coherent structures is necessary for true validation of high fidelity models and understanding of wind turbine flow physics. Alternatively, PIV is a velocity measurement technique that can capture instantaneous turbulent coherent structures, becoming one of the most popular non-intrusive velocity measurement techniques in laboratory and wind tunnel settings [19, 20]. Unfortunately, scaling PIV up to large field of views is extremely challenging since individual particles need to be resolved by the imaging device [21-23]. Even with state-of-the-art cameras and lasers, the scales of PIV are more suitable for wind tunnel applications and too limited without the use of extremely large tracer particles and working distances that become impractical for wind turbine investigations.

The current work describes the development of the Sandia Wake Imaging System (SWIS) to improve velocity measurement capabilities within the inflow and wake of wind turbines. The project seeks to demonstrate the viability of measuring the formation and development of instantaneous turbulent coherent flow structures near the rotor at temporal and spatial scales not accessible by current velocity measurement techniques. The velocimetry method chosen for use by SWIS is Doppler Global Velocimetry (DGV), also referred to as Planar Doppler Velocimetry (PDV). The DGV diagnostic was selected as a best fit for the field measurement objectives and is more suited for large area measurements of instantaneous coherent turbulent structures [24-26].

This investigation presents a scaled outdoor demonstration to bridge the technology development scale between previously conducted laboratory tests and the planned field tests to be conducted at the Scaled Wind Farm Technology (SWiFT) facility [27], which is operated by Sandia National Laboratories through U.S. Department of Energy funding. Using the imaging area as an indicator of the measurement scale, the initial laboratory experiments were conducted on a 15 cm × 15 cm viewing area, and the current intermediate-scale experiments have a 2 m × 2 m viewing area. The preliminary target for deployment at SWiFT is a 5 m × 5 m viewing area with the potential to increase to larger areas as the technology allows. The intermediate-scale set of field tests discussed in this paper incorporated system elements (such as aerosol seeding), to measure a representative flowfield (produced by a large industrial fan), that were not feasible in initial laboratory experiments yet remain more cost-effective than full-scale system refinement at SWiFT. The system signal-to-noise and measurement uncertainty limits were studied over a range of receiver signal levels (produced by varying the aerosol concentration) to calibrate the radiometric modeling used for scaling the system to larger fields of view. The results of this recent work demonstrate that a suitably scaled Sandia Wake Imaging System is capable of performing high-resolution, single-shot, quantitative, outdoor measurements of wind turbine near-wake features at the SWiFT facility. When fully implemented, this system has the potential to obtain the needed experimental data to better understand fundamental wind-turbine wake phenomena.

II. Velocity Diagnostic Selection and Background

The following section specifies some of the technical details for each of the most promising non-intrusive velocity diagnostics. These details were used in the SWIS velocity diagnostic selection process. Scanning lidar systems provide a well-established, flexible, and robust technology. Lidar systems measure the line-averaged, line-of-sight velocity component by coherently detecting the beat frequency between the transmitted laser light and the Doppler-shifted, backscattered light from naturally occurring aerosols in the atmosphere [11, 13]. Typically, the transmitted laser light frequency is shifted by an acousto-optic modulator prior to heterodyne mixing to allow the measurement of the velocity component directionality. Multiple lidar systems are required for instantaneously measuring multiple velocity components, one for each component. Several scanning patterns are possible using rotating wedge-shaped optical prisms along with synchronization across multiple lidar systems for additional velocity component measurements such as used by the Technical University of Denmark (DTU) WindScanner system [11, 28, 29]. Two general designs of lidar systems currently exist, a shorter-range continuous wave and longer-range pulsed lidar. Shorter-range continuous wave lidars have an approximate range of 10-200 m with corresponding line-averaged spatial resolution of 0.1 m to 45 m and a temporal resolution of approximately 400 samples per second [11]. The line-averaged spatial resolution, or sample volume, is a function of the laser focus length. Conversely, range gating of the receiver and laser pulse width determines the sample volume of pulsed lidars. A typical sample volume, or line-averaged spatial resolution, for a pulsed lidar is fixed by the range-gate time around 30 m over numerous range distances. Often pulsed lasers are setup to have measurement rates near 10 Hz while producing almost simultaneous velocity measurements at many incremental distances along a set beam path [29]. Pulsed lidars can have a range from 30 m to 10 km with a pointing accuracy ranging from 0.05º to 0.1º azimuth angle per meter, or 1 to 2 m pointing accuracy at a 1 km distance [28, 29].

Doppler radar technology has also successfully been employed to measure the velocity throughout wind farms, capturing wind turbine wakes, turbine-to-turbine interaction, high wind speed channels and intermittent gust propagation [4]. The innovative Texas Tech University Ka-band (TTUKA) dual-Doppler (DD) radar system delivers similar measurement capabilities to pulsed lidar systems. The range gate spacing of the radar system produces a velocity measurement spatial resolution of 9–15 m with a maximum range of 15 km and pointing accuracy of 0.05º m^{-1}. The DD radar system has a 30º s^{-1} horizontal scan rate and 0.03 m/s line-of-sight velocity accuracy. Due to these technical specifications, lidar and radar systems are extremely well suited for measuring average velocity over large areas in the vicinity of wind turbines, as previously stated, and would complement the high-resolution SWIS velocity measurements which cannot achieve such large scales.

Conversely, PIV offers a high-resolution instantaneous velocity measurement of coherent structures across smaller fields of view. PIV is based on displacement measurements of tracer particles entrained into a flowfield [19, 20]. The particle displacements are measured during a short time interval using sufficiently small particles to accurately track the flow. A thin laser sheet is normally used to illuminate the tracer particles with a pulsed laser while a camera resolves the tracer particles in subsequent image frames/pulses. The displacement vectors are typically calculated by dividing the image into small subdomains, or interrogation regions, and determining the average displacement of the particles within the region between image pairs through a cross-correlation analysis. Velocity is calculated from the displacement vectors using the image magnification, measurement plane position and time delay between pulses. Stereoscopic imaging with two cameras measures three components of the flow velocity within the planar field of the laser sheet, while planar PIV measures the velocity components normal to the light-sheet plane using a single camera. Advanced processing methods have been developed to produce high-spatial resolution measurements with low uncertainties [20].

The light scattered by the tracer particles produce an Airy disk in the imaging plane. The diameter of the Airy disk can be increased across multiple pixels by increasing the f-number (reducing aperture) of the receiver optics to avoid peak-locking errors; however, this concurrently reduces the amount of light captured [19, 20]. This relationship becomes the limiting trade-off as scales increase. High-resolution cameras help to adequately resolve the particles in the imaging plane, while shorter working distances, high-powered lasers, large-diameter particles, and intensified cameras amplify the amount of acquired scattered light. Presently, the largest PIV scales have been achieved by seeding large-diameter tracer particles into the flow since the amount of scattered light scales by the square the particle diameter and only linearly with laser power [21-23]. Conversely, large-diameter tracer particles are only suited for small-velocity-gradient flowfields due to their poor flow tracking abilities as compared with typical micron-diameter particles. Successful PIV measurements of the atmospheric boundary layer [17] and utility-scale wind-turbine tip vortices [9] have been achieved at scales not previously possible using snowflakes as the tracer particles. These measurements have provided insight into the unsteady flow structures, but they are limited by the conditions upon which data can be acquired and the fidelity at which snowflakes can adequately track the flow. These limitations are why PIV scales are more suitable for wind tunnel applications without the use of extremely large tracer particles and working distances that become impractical for wind turbine investigations.

On the other hand, DGV has the opportunity of scaling more easily to large fields of view since individual particles are not resolved [24]. The roots of DGV can be traced to the proposed combination of molecular filters and lasers to create a high spectral resolution lidar system [25, 30]. DGV measures the Doppler shift frequency (Eq. (1)) of light scattered from aerosol particles within a flowfield illuminated by a narrow linewidth laser sheet. In Eq. (1), Δf_D is the Doppler shift frequency, λ is the incident laser wavelength, $\hat{\boldsymbol{o}}$ and $\hat{\boldsymbol{\imath}}$ are the light-wave observation and incident unit vectors respectively, and $\boldsymbol{V}$ is the flow velocity [24, 25].

$$\Delta f_D = \frac{1}{\lambda}(\hat{\boldsymbol{o}} - \hat{\boldsymbol{\imath}}) \cdot \boldsymbol{V} \tag{1}$$

The bisector angle of ($\hat{\boldsymbol{o}} - \hat{\boldsymbol{\imath}}$) defines the direction of velocity sensitivity. Thus, multiple velocity components can be measured with additional observation vectors and/or multiple laser illumination directions [31]. A molecular absorption filter, typically molecular iodine contained within an optical cell (glass cylinder with optical windows), converts the Doppler shift frequency into an intensity variation measureable by cameras to produce a velocity image [30, 31]. Numerous iodine absorption lines exist within the frequency range of frequency-doubled Nd:YAG lasers. The choice of absorption line, vapor pressure, temperature, and cell length tailor the sensitivity of the finite-sloped transmission profile [24, 32]. The partial absorption, or intensity change, of the scattered light through the cell depends on its frequency and the absorption profile. The Doppler shift of the seeded particles is calculated at each pixel of the imaging device using Eq. (1), the measured intensity and camera observation unit vector, the iodine transmission profile, and the incident light-sheet-laser frequency and unit vector [30].

Both signal (filtered) and reference (non-filtered) cameras are required to remove the spatial intensity variations due to spatial inhomogeneities in the laser intensity and seeding density. A pulsed, frequency-doubled Nd:YAG laser produces sufficient scattering to yield large enough signal-to-noise ratios for instantaneous measurements. Thus, coherent turbulent structures can be resolved on a larger scale than PIV since individual particles do not need to be resolved and at a rate sufficient to resolve temporal evolution of the unsteady structures [24]. A seed laser is needed to provide single frequency (narrow linewidth) operation and back-illuminated CCD or intensified CCD (ICCD) cameras may also be required to achieve sufficient signal-to-noise-ratios. Although the DGV technology has reached a state of maturity in applications such as supersonic wind tunnel investigations [32, 33], further development is required to expand its use into wind energy related large-scale, low-velocity flowfields. This application pushes the state-of-the-art in several areas including laser technology and aerosol generation to achieve sufficient signal-to-noise ratios.

III. System Configuration

The SWIS configuration as operated during the preliminary field test is shown in Fig. 1. The Sprung structure is a temporary building that housed most of the system components including the laser system (located in a transportainer), the laser sheet optics, the fan with flow straightener, and the aerosol generation and measurement systems. The receiver cameras were housed in a specially modified van located outside of the Sprung, with a line of sight into the test area via a cargo door. The configuration of the Sprung enabled experimental testing at field scales while also controlling some key variables such as flow direction and aerosol concentration that would be difficult or impossible when operating entirely outdoors. The configuration also served to isolate the laser light for safety. Both the transportainer and van were temperature controlled to maintain equipment stability and minimize signal drift, a challenging problem when moving from the laboratory to field testing.

The flow measurement velocity requirements of the system were simulated using a 1-m diameter fan that produced a maximum axial-flow velocity of V = 16.5 m/s. The fan was located in the center of the Sprung with flow straighteners attached to reduce turbulent fluctuations (Fig. 1). Optics located in the Sprung structure transmitted a light sheet from the laser in the transportainer to an area 1.2 m downstream of the fan face (Figs. 1 and 2). The cameras imaged the light sheet, centered on the fan position, with a viewing area of 2 m × 2 m. The aerosol seeder, located upstream of the fan, produced particles with diameters between 0.5 – 10 µm (Figs. 1 and 2). The particles were introduced to increase the signal levels of scattered laser light sensed by the receiver cameras. A key objective of the test was to determine the correlation between aerosol concentration and the resulting signal-to-noise ratio (SNR) of the image data. These data, along with measurements of the ambient aerosol concentration at the SWiFT site allowed estimation of the SNR under ambient conditions as well as calculation of the required aerosol seeding to attain the SNR required for desired measurement precision.

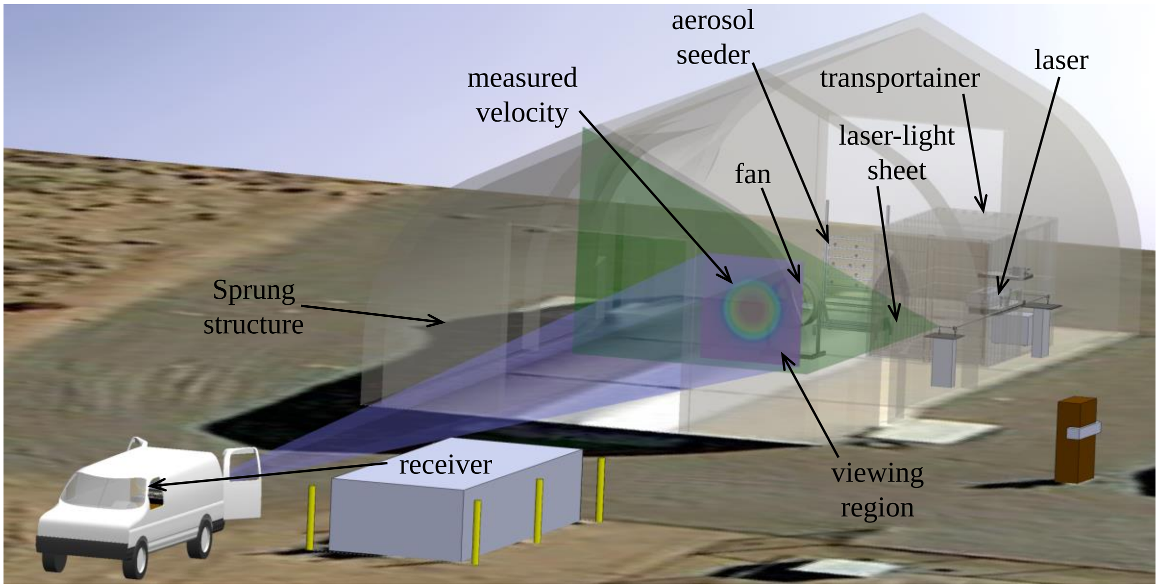

Figure 1. Schematic of the controlled field-test layout for the Wake Measurement System at Sandia National Laboratories Tech Area III showing the configuration of the major system components.

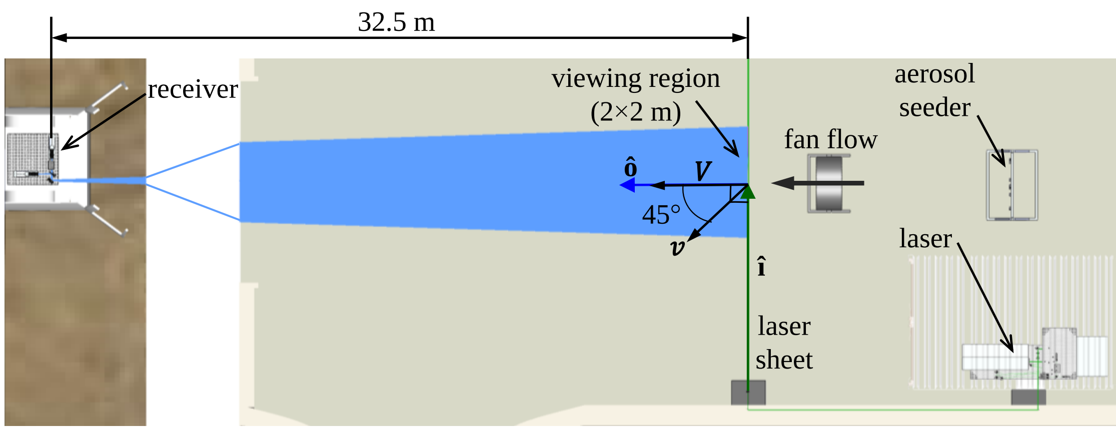

Figure 2. Overhead schematic of the measured velocity component for the measurement configuration previously described.

An overhead view of the DGV setup is illustrated in Fig. 2. As noted in Eq. (1), the bisector angle between the observation and incident laser light unit vector ($\hat{\boldsymbol{o}} - \hat{\boldsymbol{\imath}}$) defines the direction of the velocity sensitivity. In Fig. 2 the bisector angle is labeled as $\boldsymbol{v}$. Thus, the measured velocity component is at 45° to the axial flow direction ($\boldsymbol{V}$) of the fan. For this configuration the optical centerline of the light sheet is approximately in the same horizontal plane as the centerline of the receiver optics, and out-of-plane angles were not accounted for due to the long focal length and, thus, negligible effects. Future measurements will implement more precise angle calculation methods [34-37].

A. Laser Transmission System

Scene illumination for DGV was provided by a narrow linewidth, frequency stabilized, laser transmission system, shown in Fig. 3a. The laser model is a Continuum Powerlite model 9030 Q-switched Nd:YAG laser, which outputs approximately 8 ns pulses (full-width half-max (FWHM)) at a wavelength of 532 nm and a repetition frequency of 30 Hz. The pulse energy used in the experiments was about 420 mJ at the laser output aperture. The laser linewidth was narrowed by injection seeding of the master oscillator located within the Powerlite to obtain a single longitudinal mode (~120 MHz width). The laser was subsequently tuned onto the side of a strong iodine absorption feature (at 532.2418 nm) by thermally tuning the fiber seed laser.

A small portion of the laser output was picked off with an anti-reflection coated optic to measure the energy, wavelength and transmission of the beam through a reference iodine cell (Fig. 3b). The latter information was used to correct for frequency drift of the laser during data collection. Most of the beam energy was steered out of a window in the transportainer, and formed into a 1-cm-thick light sheet at the target using several cylindrical lenses. The half-angle sheet divergence in the vertical direction was 18.5 degrees illuminating a sheet with a 2 meter height at the fan. At the sheet-forming optics, the laser power was approximately 300 mJ per pulse.

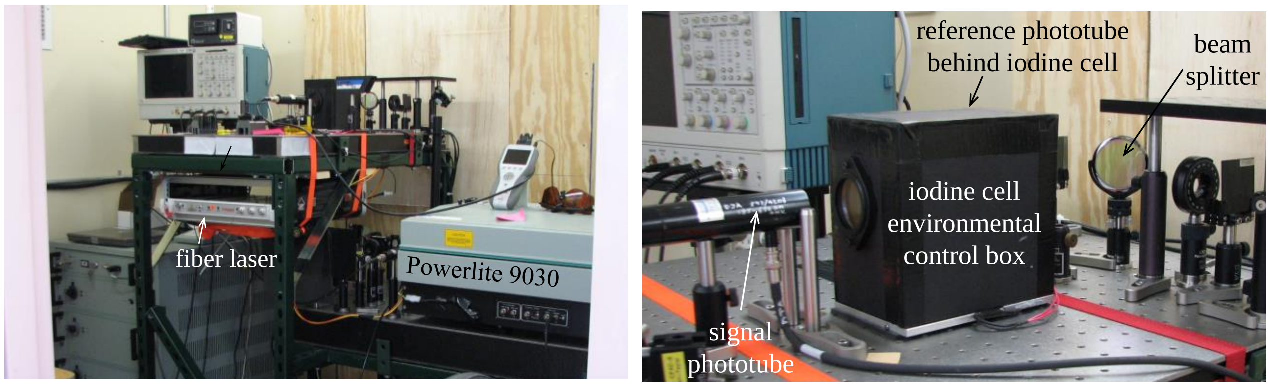

(a) **(b)**

Figure 3. (a) Image of the DGV lasers and optics, and (b) frequency monitoring system, both inside the transportainer.

In addition to gross thermal tuning, the seed laser was equipped with a frequency stabilization circuit that maintained the resonant frequency of the oscillator to be coincident with the seeding frequency of the fiber laser. Frequency stabilization was accomplished by dithering the voltage to a piezo transducer controlling the cavity length of the master oscillator on the scale of a wavelength. As a result of the cavity-length dither, even and odd pulses from the Powerlite had a very slight frequency difference. To avoid having to measure and compensate for this odd/even frequency change, data were collected at half the laser repetition frequency, or 15 Hz, which also matches the maximum frame rate of the receiver cameras when set at 256 × 256 pixel resolution.

B. Receiver System

The DGV receiver system, illustrated in Fig. 4, consisted of two intensified charge-coupled device (ICCD) cameras with 200-mm-fl f/4 lenses, a large aperture iodine vapor cell, a 50/50 beamsplitter, and a turning mirror, all mounted on a 91.44 cm × 91.44 cm breadboard. The 5-centimeter-diameter iodine cell was placed in front of the lens on one of the ICCD cameras, acting as a filter that converts changes in optical frequency (due to the Doppler shift from scattering particles) to changes in intensity. The second ICCD camera was used as a reference camera so that variations in laser illumination and/or variations in the aerosol density could be removed through ratioing images. A 50/50 beamsplitter was used to combine the line-of-sight of both cameras so they could record images without parallax. The final pointing mirror allowed fine adjustment of the signal and reference camera viewing regions when collecting data in the field. Both ICCD cameras included narrow bandpass filters centered at 532 nm to eliminate background light. The receiver assembly was built on a removable breadboard to allow alignment and characterization in the laboratory before being deployed in the back of the customized optics van. The van provided sufficient environmental protection for the receiver and made reconfiguring the receiver range and orientation with respect to the laser light sheet relatively easy. A photo of the receiver breadboard is shown in Fig. 5.

Intensified CCD cameras were chosen for the DGV system because they are extremely sensitive and can be gated on for short durations to reduce or eliminate the effect of background light. This may be especially important for the intended outdoor daytime operation of the system. The ICCD cameras, built by Andor Technologies, have 512 × 512 CCD sensors and Gen III image intensifiers. For these experiments, the receiver was positioned 32 m from the light sheet, to yield a 2 m × 2 m field of view. During data acquisition, on-chip 2 × 2 pixel binning was used to record images with 256 × 256 pixels corresponding to an 8 mm spatial resolution (at the laser sheet). Pixel binning increased the scattering signal intensity per pixel, improving the signal-to-noise ratio, and acted as a low-pass spatial filter. The images may be further binned through software methods during analysis if needed.

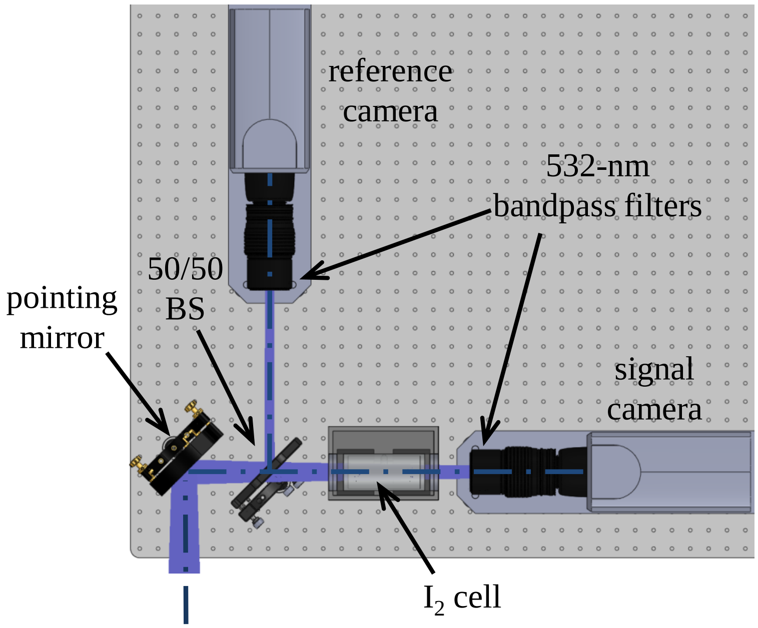

Figure 4. Schematic diagram of the DGV receiver.

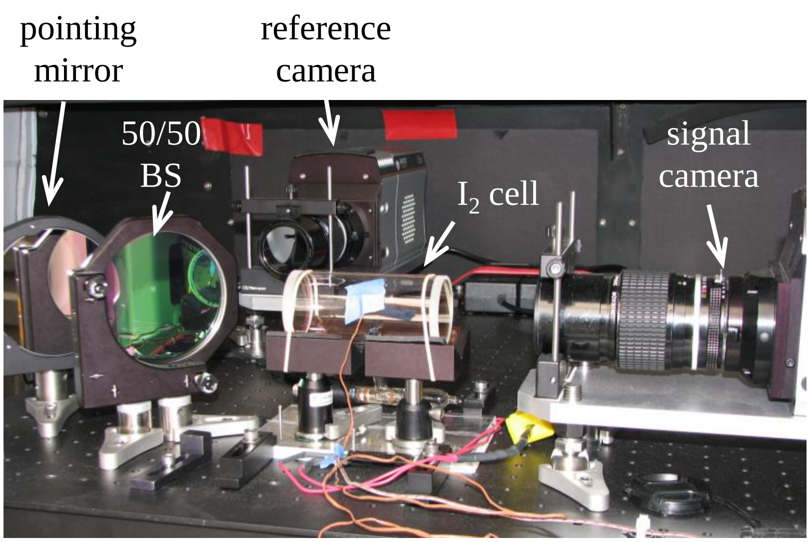

Figure 5. Photo of the receiver breadboard. During normal operation, the iodine cell is covered with an insulated box to ensure stable temperature.

The iodine vapor cell used to convert optical frequency changes into intensity changes was a 5-centimeter-diameter by 10-centimeter-long glass cell with high-optical-quality windows on the ends. It has a valve to separate the optical transmission cell volume from a side-arm (or ampule) containing iodine crystals. The valve allowed the iodine pressure to be vapor limited at ~25°C and remain constant inside the cell at any temperature above 25°C [24, 25, 31]. The iodine cell was maintained at 40°C to ensure the concentration was constant regardless of the ambient laboratory (or field) temperature. A nominally identical iodine vapor cell was used in the laser transmitter system to monitor any changes in the laser frequency during operation.

The data acquisition system for the receiver was written in LabVIEW software and consisted of two main modules: one to control the ICCD cameras and record the camera data, and another to record transmission data from the reference iodine cell in the transmitter. Both LabVIEW modules were executed on a Windows 7 desktop computer located in the transportainer with the laser transmitter. Ethernet USB extenders allowed the program to communicate with the ICCD cameras located 32 m away. An Ethernet keyboard, video, and mouse extender allowed control of the data acquisition program from either the laser room or the van containing the receiver. All of the timing and triggering electronics were located with the laser in the transportainer. The trigger signal for the ICCD cameras was transmitted over a 200-foot-long RG58 (standard 50Ω) cable.

The LabVIEW data acquisition system recorded image and ancillary data at a 15 Hz rate. On each data acquisition cycle, the system recorded a pair of images, one from each ICCD camera, along with transmission data from the reference iodine cell on the laser. For each data run, consisting of a contiguous series of images, the system recorded all the relevant camera and instrument settings and a text file with operator-supplied comments. The data were processed offline using MATLAB code (described in Section IV).

C. Fan System

The flow field was produced using a one-meter-diameter, 3.7-kW axial-flow fan capable of moving 650 cubic-meters-per-minute and producing a peak velocity of 16.5 m/s (Fig. 6). The fan size was selected such that the entire fan wake would fit inside the imaging area. The fan power and maximum velocity were limited by the practical limits of an off-the-shelf system that would work on the available power supplied to the Sprung structure. A programmable inverter was added to the system so that the fan speed could be varied up to full power. A flow straightener was assembled using a plastic material with square openings of size 2 cm, and channel length of 16.25 cm. The straightener was observed to drastically reduce the turbulence intensity in the wake of the fan, thus reducing the sampling time required to produce repeatable data.

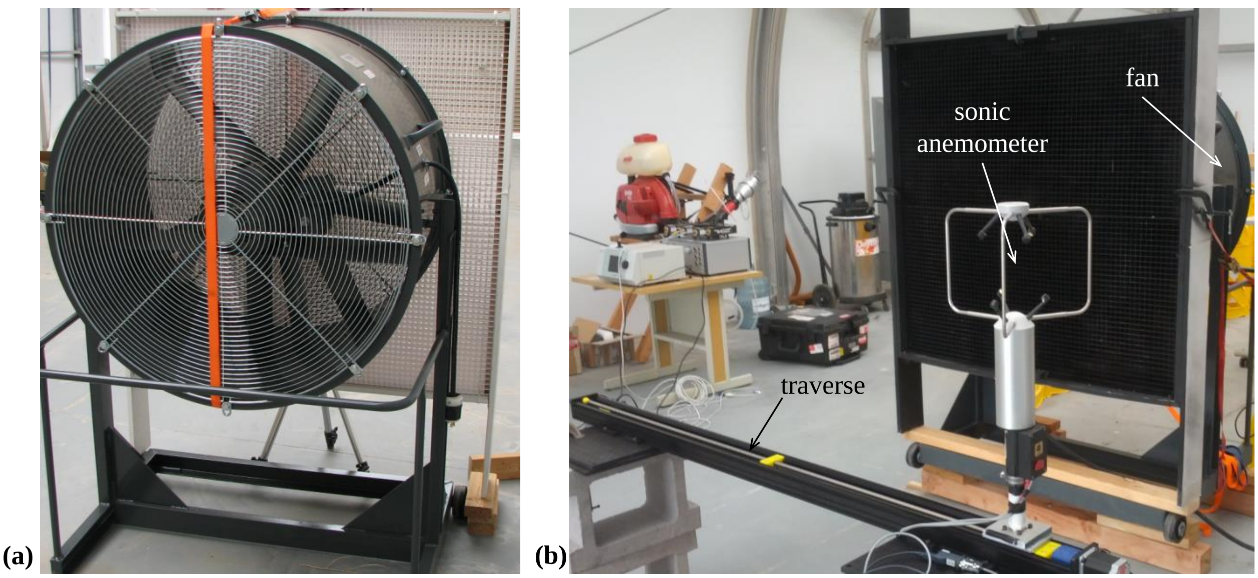

Figure 6. Fan (a) with flow straightener attached, and (b) sonic anemometer mounted on a linear traverse.

The baseline flow-field measurements were taken using a Young 81000 ultrasonic anemometer. The sonic anemometer has a cylindrical sample area of 10 cm high with a 10 cm diameter and has a specified accuracy of ±0.1 m/s. The anemometer was mounted on an automated linear traverse and controlled with a LabVIEW-based data acquisition system to automatically sample the flow. Wake velocity measurements were sampled digitally from the sonic anemometer at 32 Hz and averaged over 30 second bins. The fan and measurement system are shown in Fig. 6.

D. Aerosol System and Scattering Efficiency Characterization

Two aerosol generation systems were evaluated for use in the Sprung structure. The first system used a smoke generator to produce mineral oil particles. Although the mineral oil particles were effective in scattering light for the Doppler measurement, smoke generation was not deemed to be scalable to SWiFT-site scale both due to cost and complexity of the equipment needed for such large scale deployment. Moreover, the particle size distribution of the mineral oil aerosol changed over time due to evaporation, thereby changing the optical scattering cross section. The second set of experiments was conducted with KCl particles that were equally effective in providing scattering particles while being readily scalable to large-scale outdoor scenarios. The KCl aerosol particle size distribution was stable over time and did not vary with concentration.

The KCl aerosol generator consisted of an array of up to 12 agricultural spray nozzles that produced a fine mist of KCl/water solution about 6 m upwind of the fan (Fig. 7). This distance is sufficient to allow the liquid to completely evaporate, leaving small KCl particles entrained in the flow. For the small volume of the Sprung structure, three nozzles were sufficient to produce aerosol concentrations greater than 5000 particles/cm^{-3}. A solution of 10 g KCl per liter of water dispensed at 15 ml/minute/nozzle produced a mist of ~15-μm-diameter liquid droplets which dried out to produce ~1-μm-diameter solid KCl particles.

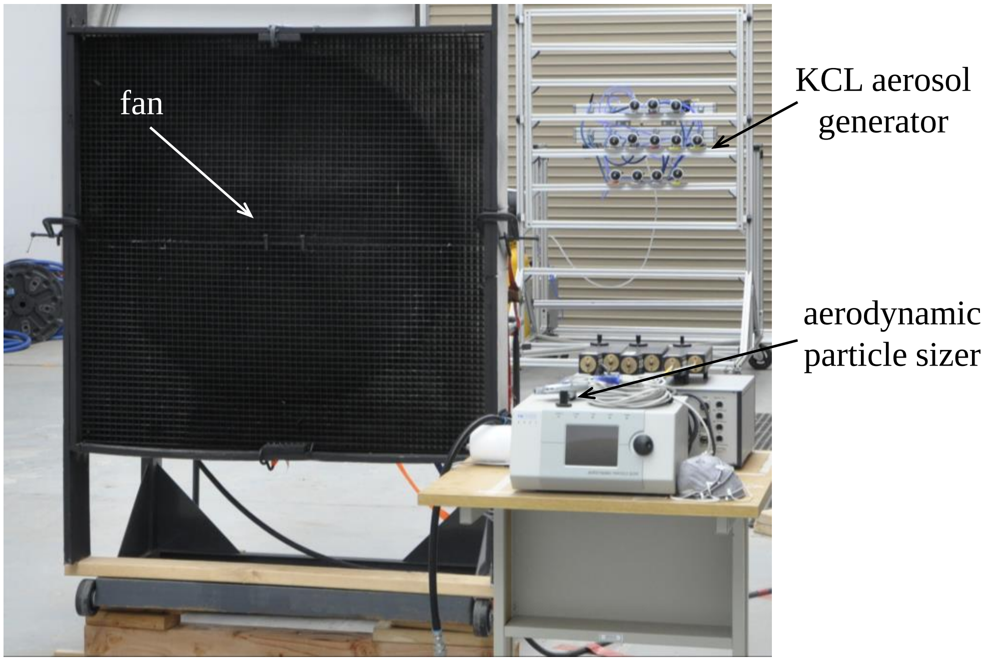

Figure 7. Experimental setup of KCL aerosol generator, fan, and aerodynamic particle sizer.

A computational lidar model was developed to predict the performance of the DGV system under a variety of conditions, taking into account the aerosol concentration (either natural or artificially produced), laser energy, laser sheet size, receiver field of view, receiver standoff distance, receiver lens aperture, among other parameters. One of the important parameters in any lidar model is the differential scattering cross section which accounts for the scattering efficiency of the aerosol particles. Measured backscatter cross sections for Arizona Road Dust were used in the preliminary calculations since Arizona Road Dust is a standard material used to simulate naturally occurring dust in the environment. Later, the DGV instrument was used to directly measure the response of the receiver cameras under well-controlled experimental conditions both to validate the initial differential scattering cross section assumptions and to obtain direct data which were used for the scaling of new configurations (such as SWiFT site deployment). To quantify the scattering efficiency (differential cross section) and validate the radiometric lidar model, experiments were conducted in which the Sprung shelter was filled with a spatially uniform concentration of artificially generated aerosol (first mineral oil smoke and later KCL particles) and the response of the ICCD camera system was measured as the concentration of the aerosol was varied.

The concentration and size distribution of the KCl aerosol were measured using a TSI model 3321 aerodynamic particle sizer (APS) located near the fan. The mean particle size distribution (PSD) for this series of experiments is shown in Fig. 8. The shape of the PSD was remarkably consistent over a wide range of concentrations achieved during the tests. Although this PSD peaks near 0.6 μm, larger sizes may be possible by increasing the KCl solution concentration. Somewhat larger particles may be beneficial since the scattering cross section scales (approximately) as the cross sectional area of the particles.

To allow use with radiometric models, the differential scattering cross section was computed using a Mie scattering code implemented in Matlab [38, 39]. The primary input was the measured PSD. At 90°, the computed differential scattering cross section is 3.2×10^{-10} cm^2/sr. This cross section varied by less than ±2% over the series of measurements, indicating a very consistent PSD over the wide range of concentrations used in these experiments.

The computed differential scattering cross section also agreed well with the experimentally determined cross section using the experiment geometry, laser power, aerosol concentration, and receiver sensitivity. The number of photons collected at the receiver was calculated from the analog-to-digital (A/D) counts measured by the cameras using the Andor-measured sensitivity specifications and correlated with measured aerosol concentration.

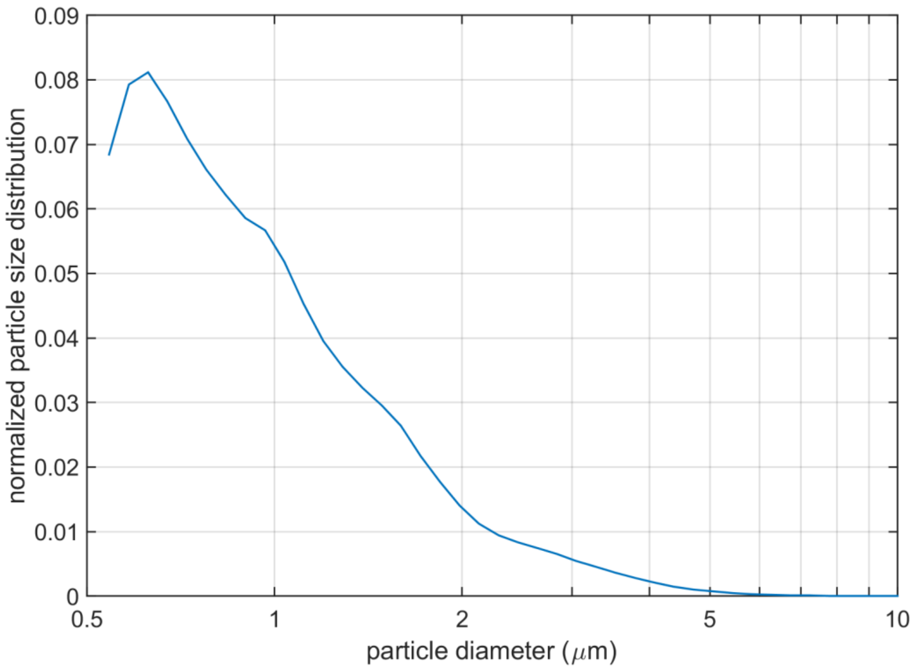

Figure 8 Mean, normalized particle size distribution for KCl seeding experiments.

IV. Data Processing

A number of data processing steps were required to obtain the velocity images presented in Section IV from the raw data. The data processing steps include image flat fielding to correct for non-uniformity in camera sensitivity, image registration to align slight differences in the field of view between cameras, intensity-to-frequency conversion, and removal of the laser frequency variation across the field of view [24, 25, 32].

A. Image Flat Fielding

Image flat fielding is a process to correct for the spatial non-uniformity in sensitivity of ICCD camera images. Figure 9 shows the raw response of the signal and reference ICCD cameras to a uniformly illuminated scene (provided by an integrating sphere) along with the corresponding corrected images. The spatial non-uniformity observed in the uncorrected images is the result of an inherent non-uniform response of the image intensifier, and to a lesser degree, the CDD itself. The circular feature prominent in both uncorrected images is likely the result of accidental overexposure to a fixed, circular calibration target and subsequent degradation of the photocathode response in this area. Fortunately, the difference in sensitivity is relatively small and the image flat-fielding process completely removes the spatial variation during processing (Fig. 9). The darkfield images of the signal and reference cameras were removed prior to flat-field processing. Background images were not obtained due to the negligible accumulation of background intensity over the short 30 ns open gate time.

A 30.48-cm-diameter integrating sphere provided a uniform illumination source for the receiver optics (the signal and reference cameras, beam splitter, and iodine cell) for calibrating/deriving the flat-field image corrections (Fig. 10). The intensity of the laser into the integrating sphere was varied to cover the dynamic range of the cameras, while a linear photodiode provided a relative intensity calibration. The correction function for each pixel was calculated using a least-squares spline fit that covered the dynamic range of the cameras and provided simultaneous image flat fielding and non-linearity correction [40]. The corrected and uncorrected responses of the signal and reference camera are displayed in Fig. 10.

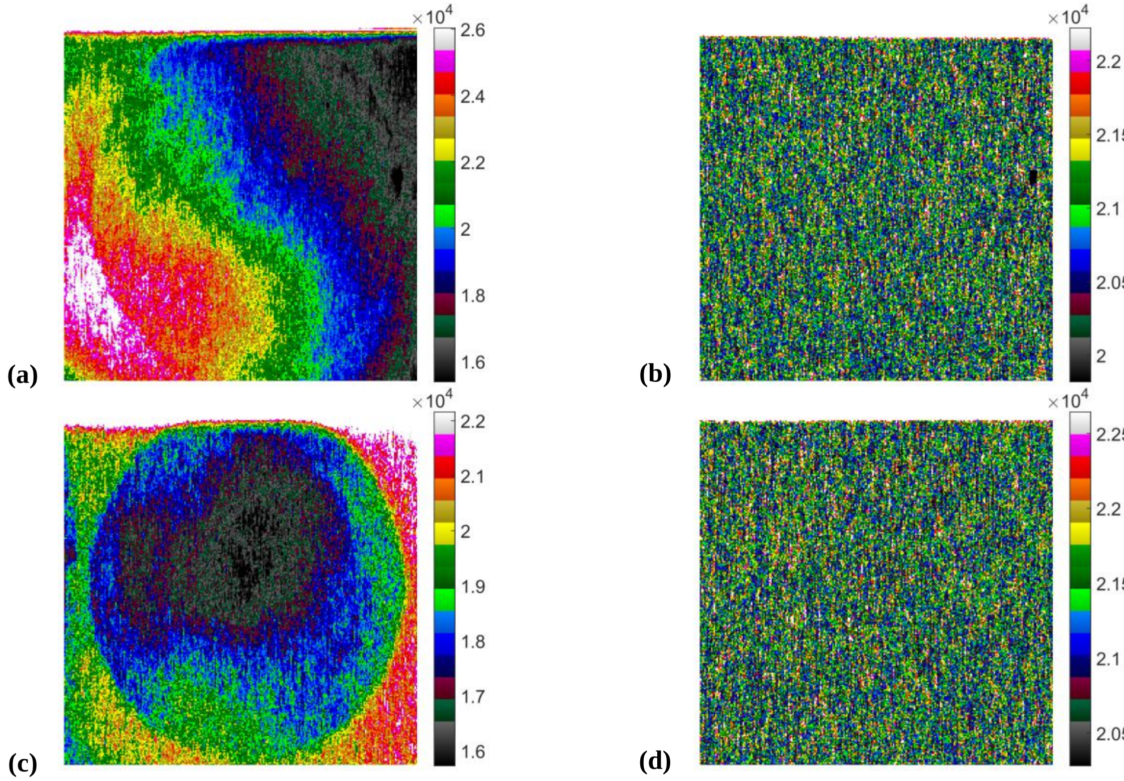

Figure 9. Camera spatial non-uniformity in counts: (a) uncorrected signal camera,(b) corrected signal camera, (c) uncorrected reference camera, and (d) corrected reference camera.

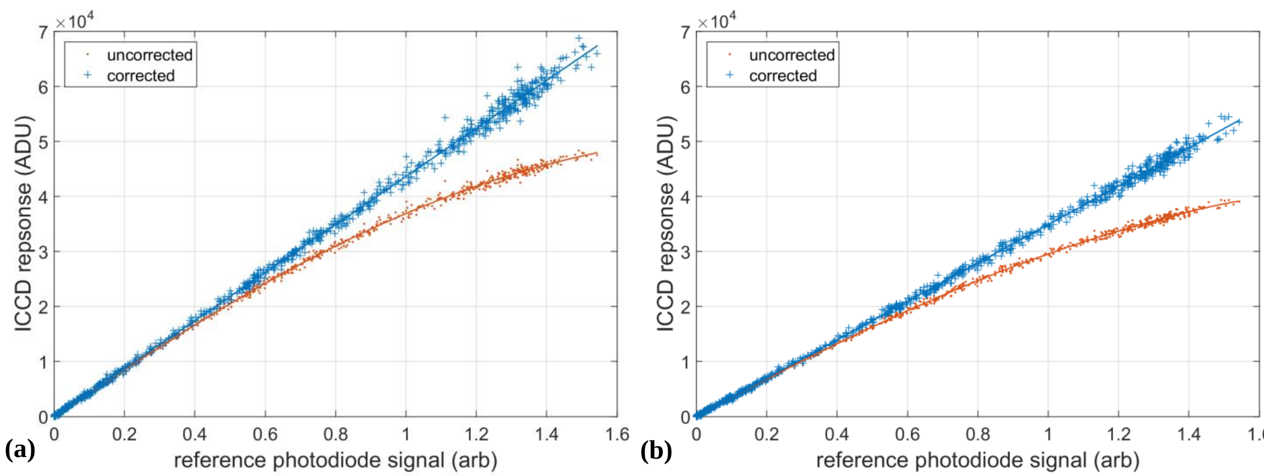

Figure 10. Uncorrected and corrected ICCD response of the center pixel (128, 128) in analog to digital counts with a gain setting of 3000: (a) signal camera, and (b) reference camera.

B. Image Registration and Intensity Flat Fielding

The next step in processing was image registration and geometric transformation. The signal and reference cameras were closely aligned using a large registration target, though small variations between the camera viewing regions remain. Thus, image registration and geometric transformations were employed to correct any additional changes in relative alignment. The image registration between the signal and reference cameras was calculated in two steps using an instantaneous image. First, a two-dimensional phase correlation of intensity was used to calculate pixel alignment of the reference image with respect to the signal camera image. Next, an intensity-based parent-child optimizer iterated on geometric transformations using bilinear interpolation to converge on sub-pixel alignment between images. Once the final image registration was obtained, the remaining reference images were bilinear interpolated to align with the corresponding signal images.

Flowfield images acquired with the laser tuned outside of the iodine absorption line (full transmission where Doppler shifts do not create an intensity change) provide a normalization to correct sensitivity variations due to optical path differences between the signal and reference cameras [24]. The pixel-by-pixel normalization process by the average out of the absorption line (out-of-line) images is referred to as the intensity flat fielding step, not to be confused with the previously described image flat fielding step. The average intensity flat field normalizes sensitivities with respect to each optical leg (or path) of the receiver optics, and corrects any small shift from the 50/50 beamsplitter caused by polarization variations in the scattered light, although the variations should be small since the beamsplitter is polarization insensitive.

C. Intensity-to-Frequency Conversion

The measured absorption profile, for both the camera and laser frequency monitoring cell, converts the intensity variation into a frequency shift using the finite-slope absorption profiles displayed in Fig. 11. The absorption profile, or frequency-to-intensity conversion, can be tailored by choice of iodine absorption line, cell length, vapor pressure and temperature. The current absorption profiles (Fig. 11) were selected and tailored to maximize system sensitivity. Various methods exist to calibrate the frequency-to-transmission transfer function of iodine cells. Given the available equipment, the use of a known velocity target was identified as the most accurate method for measuring the iodine absorption profile. A spinning wheel with known frequency shift was used to calibrate the frequency-to-transmission transfer function, displayed in Fig. 11 [41]. The frequency shift of the spinning wheel did not cover the full range of iodine line transmission. This limitation was overcome by piecing together numerous incident laser frequencies along the iodine line, with a least-squares method. Figure 11 shows the final absorption line profile, fit using an absorption model developed by Forkey [42] to the composite data points of the spinning wheel as a function of cell temperature and vapor pressure. The absorption model was only used as the spline-fitting function over the spinning wheel data points on the side of the chosen absorption line. The sensitivity of the absorption line (dT/df) was found to be 0.27 %/MHz along the linear portion of the profile. Incidentally, the sensitivity profile also depends on the laser linewidth and must be re-measured if a different laser (with different linewidth) is used in the DGV system.

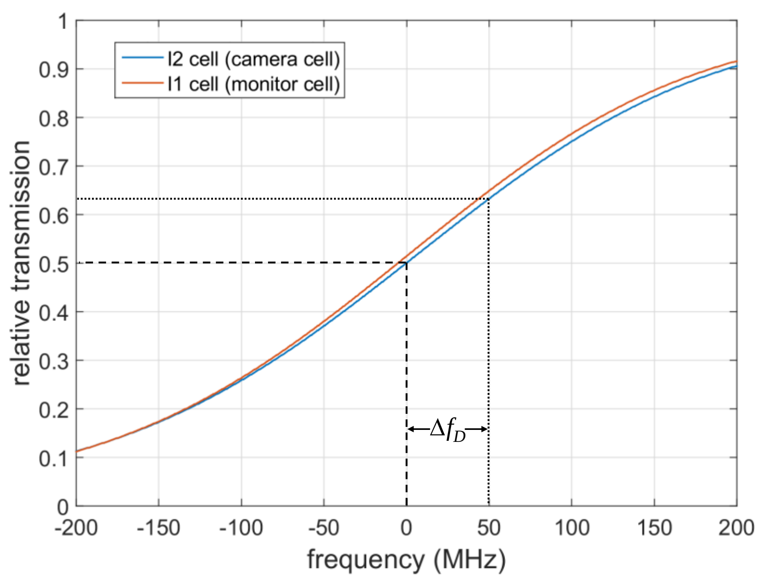

Figure 11. Iodine absorption profile for the camera and laser monitoring cells.

Next, the transmission profile displayed in Fig. 11 was used to convert the relative transmission of each pulse into a laser frequency (Fig. 12). As mentioned in Section III.A., the laser-frequency-monitoring system (Fig. 3b) tracks the frequency drift of the laser pulse-by-pulse during data collection, as shown in Fig. 12. Accurate Doppler shift measurements require knowledge of the incident laser frequency obtained from the reference system that could otherwise be misinterpreted as velocity changes [30].

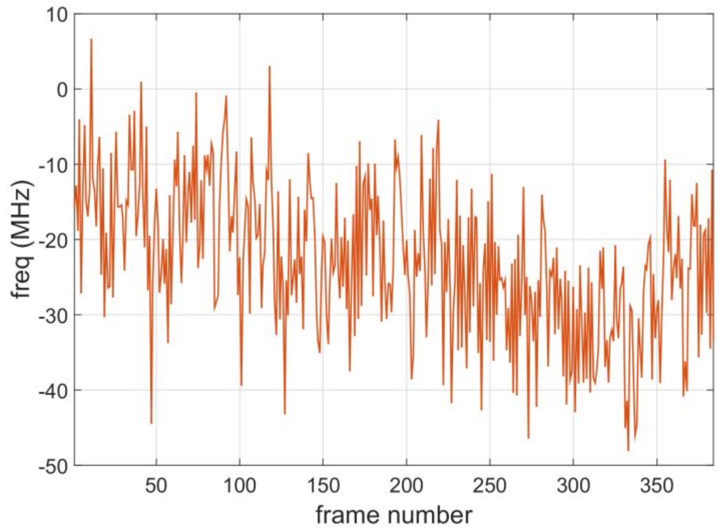

Figure 12. Monitored laser frequency drift pulse-to-pulse over 384 frames.

D. Removal of Spatially Varying Laser Frequency

The laser has additional frequency variation across the spatial profile of the beam or sheet. When imaging a target or scene with uniform velocity, the spatially varying frequency of the laser beam results in a velocity gradient in the processed velocity image, as displayed in Fig. 13. The mechanism that causes the spatially varying frequency across the laser beam is uncertain but is believed to be due to dynamic gain saturation within the Nd:YAG rod [43]. The light intensity across the laser beam (plane normal to incident laser unit vector) also produces subtle variations from pulse-to-pulse [26, 44]. However, this intensity variation is obscured in Fig. 13 because it is integrated by the thickness of the laser sheet.

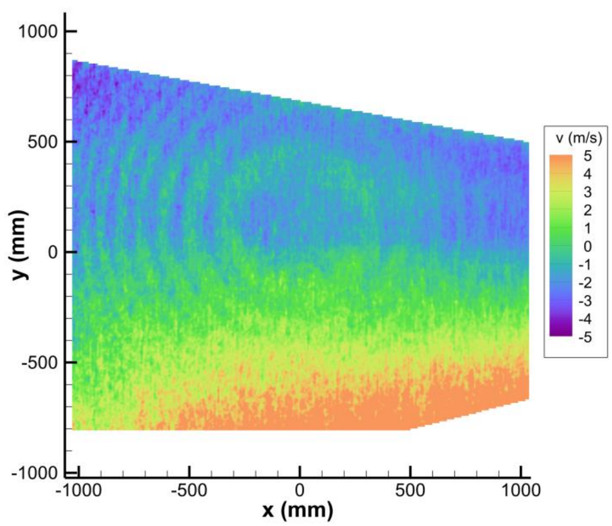

Figure 13. Spatial frequency variation of laser within viewing region displayed as an equivalent velocity.

The laser intensity and frequency spatial variations created challenges while using the spinning wheel target for iodine line absorption calibration and image alignment. The frequency variation presents a particularly troubling technical challenge for the system implementation at the SWiFT facility since the incoming flow rarely has zero velocity. Even during the current experiments a bias velocity existed due to the fact that the aerosol seeding nozzles created a circulation and non-zero background velocity. One possible solution is to use a laser that is frequency stable enough to not require a zero-velocity correction. An example would be a tunable narrow linewidth amplifiedlong-pulse Nd:YAG laser, similar to a specifically tailored pulse-burst laser [31], in order to maintain frequency stability while allowing accumulations on the gated ICCD cameras without acquiring excessive background light [45-48].

The velocity bias due to the spatially varying laser frequency can be corrected by subtracting a frequency flat field from the Doppler frequency data [24]. Frequency flat field images are created by measuring the viewing region with the laser-frequency tuned into the absorption line without the presence of a Doppler shift (zero velocity), shown in Fig. 13. A fringe pattern created in the signal camera from the iodine cell is clearly visible in Fig. 13 overlaid on the laser frequency pattern. This pattern can be readily eliminated in future designs by utilizing cell windows with an increased wedge. Subtracting the frequency flat field images from the Doppler images also helps minimize the fringe pattern effects which arise primarily from the iodine cell optics.

E. Velocity Image Calculation

Three data sets were required to process the velocity images, remove the previously described image distortions, and reduce measurement uncertainty:

1. Images were acquired with the fan on and laser tuned in the absorption line near 50% transmission to produce an intensity ratio image of the Doppler shift frequency, referred to as $\Gamma_D = I_s/I_r$ where the subscripts s and r refer to signal (iodine cell) and reference images, respectively, I is the image intensity in A/D counts, and the D subscript referrers to the Doppler shift data set.

   Simultaneously, the laser frequency monitoring system measures the pulse-to-pulse transmission through a reference iodine cell. The ratio $\gamma_D = i_s/i_r$ is the ratio of the laser energy that passes through the reference iodine cell to the incident laser energy. The subscripts s and r refer to signal (iodine cell) and reference phototubes, respectively, and i is the integrated phototube signal with arbitrary units.

2. Frequency flat-field/background images were acquired without flow and with the laser tuned to 50% transmission to produce the image and laser intensity ratios $\Gamma_b = I_s/I_r$ and $\gamma_b = i_s/i_r$, where b represents the frequency background which will be subtracted from the Doppler shift frequency to remove the spatial frequency variation and reduce measurement bias.

3. The intensity flat field images were acquired without flow and the laser tuned out of the absorption line (100% transmission) to produce the image and laser intensity ratios $\Gamma_f = I_s/I_r$ and $\gamma_f = i_s/i_r$, where f represents the intensity flat field used to normalize the ratios to relative transmission of the iodine line and minimize intensity variations due to optical path differences between signal and reference devices.

The raw images were then processed using the three sets of data and MATLAB scripts in the following manner [24]:

1. All acquired images were corrected for spatial non-uniformity and non-linearity using the image flat-fielding process shown in Figs. 9 and 10.

2. The signal and reference images were aligned using image registration and geometric transformations of the reference image by means of bilinear interpolation.

3. The Doppler shift image and phototube ratios were normalized by the respective intensity-flat-field ratios:

$$T_D = \frac{\Gamma_D}{\Gamma_f} \text{ and } t_D = \frac{\gamma_D}{\gamma_f} \tag{2}$$

4. The frequency background image and phototube ratios were normalized by the respective intensity-flat-field ratios:

$$T_b = \frac{\Gamma_D}{\Gamma_f} \text{ and } t_b = \frac{\gamma_D}{\gamma_f} \tag{3}$$

5. The Doppler image and phototube relative transmission ratios were converted to frequency using the intensity-to-frequency transfer functions plotted in Fig. 11 for both the camera (H_c) and phototube (H_p)

iodine cells. Next, the frequency shift was calculated by subtracting the laser frequency (obtained using the phototubes Fig. 12) from the image ratio frequency:

$$\Delta f_D = H_c(T_D) - H_p(t_D) \tag{4}$$

6. The calculation in step 5 was also performed on the frequency background data:

$$\Delta f_b = H_c(T_b) - H_p(t_b) \tag{5}$$

7. The final Doppler shift image was corrected by subtracting the laser spatial frequency variation from the Doppler shift frequency image:

$$\Delta f_{D,corrected} = \Delta f_D - \Delta f_b \tag{6}$$

8. By rearranging Eq. (1) the velocity of the fan was calculated from the corrected Doppler shift frequency. With the current optical setup $(\hat{\boldsymbol{o}} - \hat{\boldsymbol{\imath}}) = \sqrt{2}$ and λ = 532.242 nm, producing the final velocity images along the velocity sensitive vector:

$$v = \frac{\lambda}{\sqrt{2}} \Delta f_{D,corrected} \tag{7}$$

V. Flow Imaging Results

The image in Fig. 14a displays the velocity flow field averaged over 384 frames (approximately 26 seconds) of the 1-m diameter industrial fan set to maximum power. The image area is approximately 2 m × 2 m with regions outside the laser sheet removed for clarity. The current system configuration, with one set of receiver cameras, captures a single component of the flow velocity as illustrated in Fig. 2 (45° component from fan axis). As expected, the average velocity image reveals an annulus of greater velocity produced by the fan. The increased velocity along the top and right side of the annulus is likely from a fan induced clockwise swirl captured in the measured velocity component. The measured velocity component also creates an increase in velocity along the outer-shear layer on the right side with a corresponding decrease on the left. Figure 14b presents an instantaneous (single shot) velocity

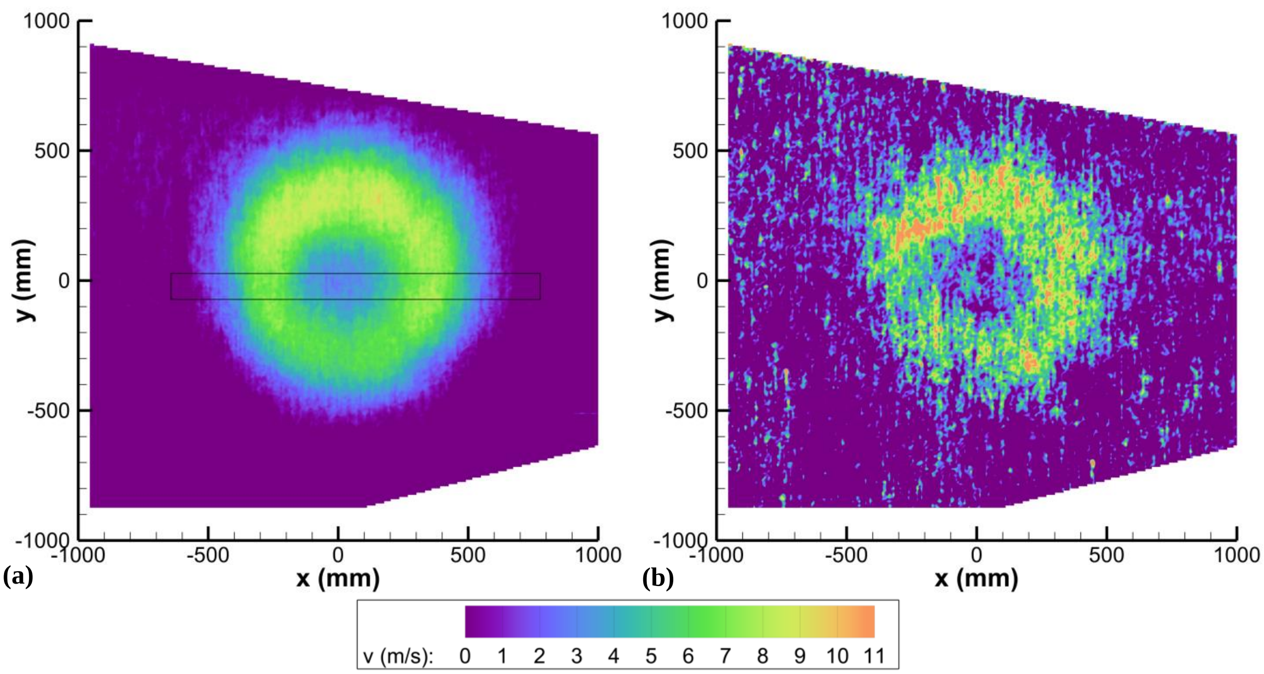

Figure 14. Wake imaging velocity image of fan flow at 2 m × 2 m viewing area with no/low laser signal regions removed: (a) average and (b) instantaneous.

image taken from the ensemble of 384 images averaged in Fig. 14a. The signal levels result in a noisier instantaneous velocity image with a noise level of approximately ±3.3 m/s. However, additional flow structures can be observed in the instantaneous image due to turbulence produced by the fan. A noise level of ±1.8 m/s was achieved during a zero-velocity data set with an average aerosol concentration of 3600 cm^{-3}.

To validate the average measurement, a sonic anemometer was used to obtain independent velocity data for comparison with SWIS (Fig. 15). Velocity averaged over 30 seconds was measured at discrete points along the center line of the fan with a resolution of 10 cm × 10 cm using an automated traverse. To compare between the data sets, the boxed region of the velocity image in Fig. 14a indicates the spatial area that was sampled from SWIS data to match the sampling area of the sonic anemometer. As depicted in Fig. 15, good agreement exists between the two velocity measurement methods with a maximum difference of approximately 0.6 m/s in the low-velocity center region of the fan wake. The increased velocity along the center is most likely due to the velocity added by the KCl spray nozzles which were not operated during the sonic anemometer measurements. Additional data sets produce a similar comparison with the sonic anemometers. However, a velocity bias does appear to exist as an offset in the measurement. The bias is approximately -0.2 m/s, but can vary between data sets. As previously described, the velocity bias is probable due to a non-zero background velocity, possibly created by the aerosol seed system.

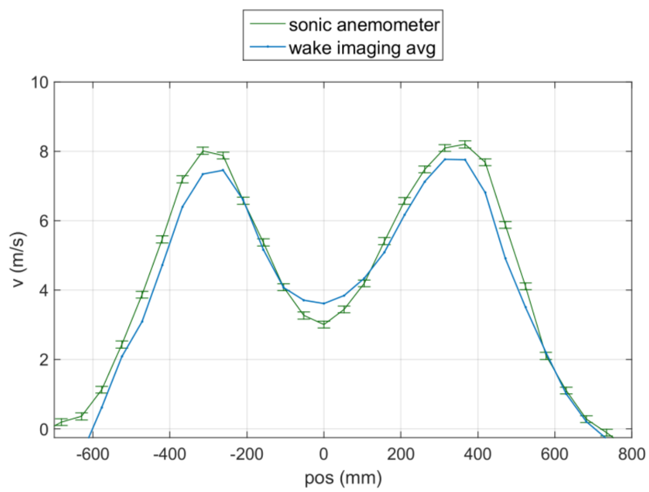

Figure 15. Comparison of average sonic anemometer measurement with SWIS over area indicated in Fig. 14.

VI. Discussion

A. Noise Equivalent Velocity

Velocity uncertainty can be described by a noise equivalent velocity (v_{neq}), similar to how noise equivalent power (NEP) is commonly defined for discrete detectors. Both systematic and random errors contribute to uncertainty. The uncertainty of the velocity measurement depends on the accuracy of the laser frequency, measurement of the scattered light, and a well-characterized intensity-to-frequency transfer function [24, 25, 41]. An error due to iodine cell calibration [41], laser speckle [26, 49, 50], noise sources [51-53], iodine filter temperature sensitivities [24], laser reflections [54], and background light [32] can all contribute to uncertainty in the velocity data.

The noise sources in the DGV system include laser frequency noise, camera read noise, excess noise from the intensifier gain, and noise associated with the signal processing algorithm. Past studies have attributed the dominant noise source to laser speckle [26, 49], while others have found it to have less of a contribution based on increased measurement area and lower flow velocity [50]. With sufficient signal at the current measurement area and flow velocities, the performance of SWIS is most likely limited by shot noise of the signal photons. Assuming the shot noise is correlated between the signal and reference optical legs of the receiver and that the shot noise and ICCD noise factor (F) are the dominate noise sources, the corresponding noise of the normalized Doppler shift intensity ratio, T_D (Eq. (2)), reduces to Eq. (8), where $\Gamma_D = I_s(\lambda_D)/I_r(\lambda_D)$, camera intensity is $I_s(\lambda_D) = G_s\eta_s N_s(\lambda_D)$, G_s is the signal camera gain, η_s is the signal camera quantum efficiency, and N_s is the number of photons per pixel at the signal camera. The corresponding noise equivalent velocity simplifies to Eq. (9), assuming that the noise of the intensity flat-field and frequency background go to zero since they are averaged quantities. From Eqs. (8) and (9), it becomes clear that the v_{neq} approaches zero as the ratio of photoelectrons between the signal and reference receiver legs approach one. Thus, the shot noise can be reduced by altering the transmission/refection ratio of the beam splitter. This same relationship was also found by Fischer et.al. [51] for conventional DGV configurations. Future experiments are planned to confirm the beam splitter ratio optimization found through shot noise analysis. The iodine cell losses correspond to an optimized beam splitter ratio of approximately 65/35 with respect to the signal/reference receiver legs.

$$\sigma_T = \frac{\sqrt{F}}{\sqrt{\eta_s N_s(\lambda_D)}} \frac{\Gamma_D}{\Gamma_f} \left(1 - \sqrt{\frac{\eta_s N_s(\lambda_D)}{\eta_r N_r(\lambda_D)}} \right) \tag{8}$$

$$v_{neq} = \left(\frac{dT}{df}\right)^{-1} \frac{\lambda \sigma_T}{2 \sin\left(\frac{\alpha}{2}\right)} \tag{9}$$

Figure 16 shows the shot-noise limit of the noise equivalent velocity for two different scattering geometries: 1) backscatter, where the illuminator and receiver are co-located, and 2) 90 degree scattering, where the illumination source and receiver are located at a right angle relative to the scatterers (Sprung configuration shown in Figure 2). The theoretical v_{neq} lines assume an ICCD noise factor of $F = 2$, which was found to be consistent with similar Andor camera models.

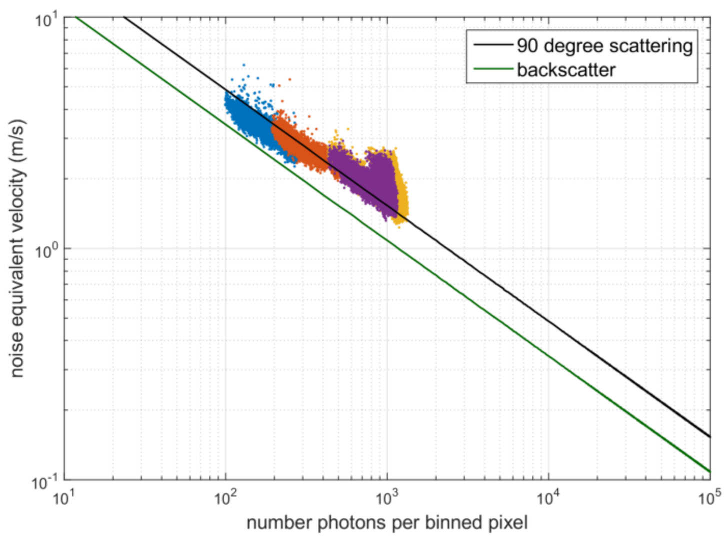

Figure 16. Noise equivalent velocity vs. the number of photoelectrons collected per 2 × 2 binned camera pixel for two different scattering geometries with experimentally measured velocity noise superimposed.

v_{neq} represents the minimum resolvable velocity variation measureable with SWIS, and depends inversely on the square root of the number of photoelectrons collected per pixel, or superpixel (binned pixel). The data points included in Fig. 16 are experimental values of v_{neq} determined from four velocity images with the flow source (fan) turned off. Each data point represents the root-mean-square (rms) noise velocity for a single pixel over the 384 frame ensemble. The corresponding number of photons was calculated from the average pixel intensity using the Andor sensitivity specifications for each camera. The variable signal level naturally occurred due to non-uniform illumination of the target plane. The trend clearly follows the theoretical curve, indicating a near shot-noise limited measurement for the setup employed.

Figures 17a and 17b show the measured v_{neq} vs. the number of single shot averages, derived from the processed zero-velocity (frequency background) image data described in Sections IV.D and IV.E. The average v_{neq} data plotted in Fig. 17 was calculated by averaging the noise equivalent velocity images (examples in Fig. 18) over a 128 × 128 binned pixel region at the center of the viewing area. Figures 17a and 17b display the trends both without and with spatial filtering, respectively.

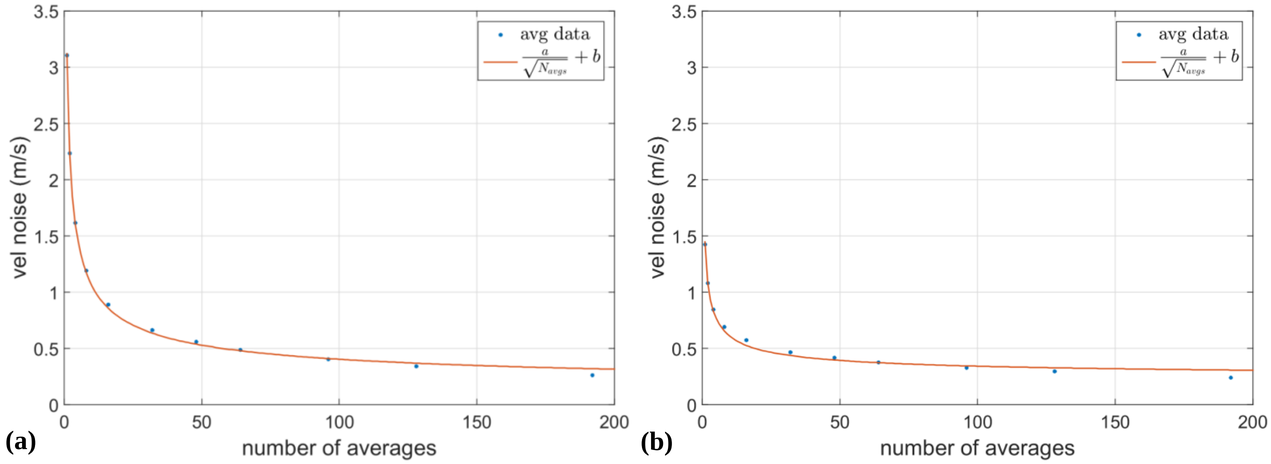

Figure 17. Average noise equivalent velocity at the center of the viewing region vs. the number of shot averages: (a) no spatial filtering, and (b) 5 × 5 averaging filter.

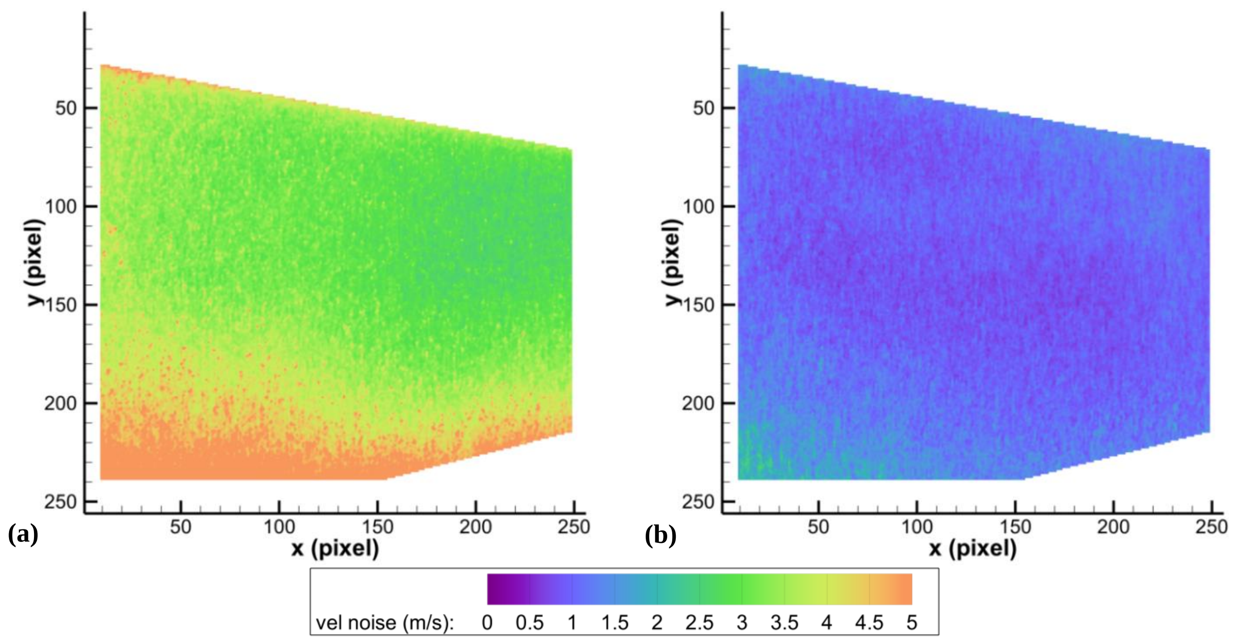

Figure 18. Noise equivalent velocity at each binned pixel throughout viewing region:(a) single shot and (b) 16 images averaged

For the chosen image, we find that v_{neq} without spatial filtering is approximately 3 m/s for a single shot (Fig. 18a), decreasing to about 1 m/s for a 16 shot averaging (Fig. 18b). Thus, conditional pulse averaging may work for certain flow structures of interest, but not all. A lower single shot v_{neq} would be required to capture faster-moving, non-coherent tip flow structures (those that do not reproduce spatially at the turbine blade passing frequency). Alternative post-processing techniques similar to those used by mature velocity diagnostics, such as PIV [20], may help to reduce noise, especially for instantaneous data. Example algorithms include outlier removal, non-linear filtering, and interpolation. Figure 19 shows the instantaneous velocity image from Fig. 14b after using a proper orthogonal decomposition filter to remove the higher order spatial scales [55]. The technique shows promise with a more rigorous validation still required.

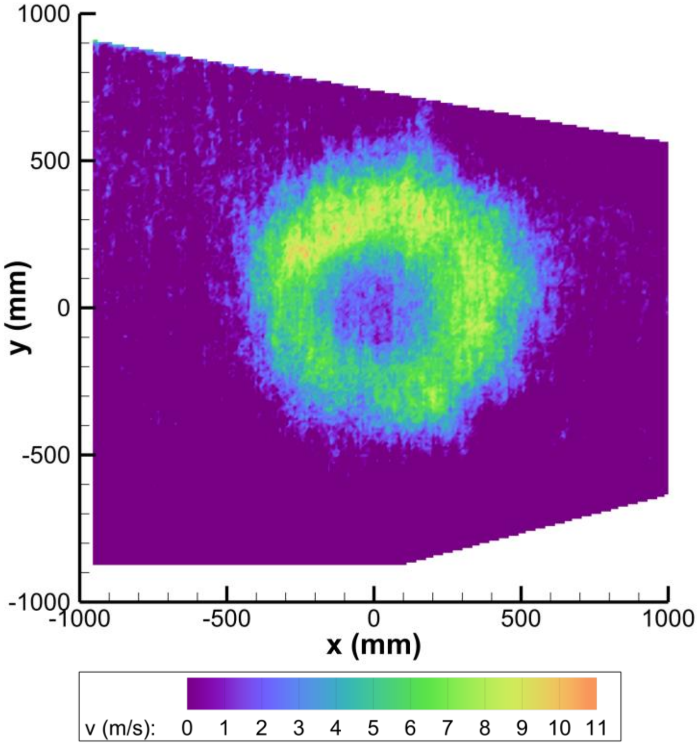

Figure 19. Instantaneous velocity images of fan flow using proper orthogonal decomposition to reduce velocity noise [55].

B. Sandia Wake Imaging System Planned Deployment at SWiFT

The goal of the planned field deployment of the Sandia Wake Imaging System at the SWiFT facility is to characterize the coherent tip vortices generated in the near-wake of a wind turbine. This goal will be accomplished by collecting high resolution velocity data in the wake, synchronized with data representing the atmospheric conditions and the operational parameters of the wind turbine. Later research will investigate the wake processes that lead to the turbulent far-wake, including the effect of atmospheric turbulence and shear on vortex stability and merging.

The most straightforward SWIS configuration for the SWiFT site is shown in Fig. 20. The laser and receivers are located on the ground with the laser sheet directed vertically, perpendicular to the rotor plane and in line with the turbine tower. One to three receivers image a 5 meter wide light sheet from the sides at a range of approximately 63 meters. Tip vortices, forming a triple helical shape about the rotor axis, propagate down range near the average wind speed and travel across the light sheet during a measurement set. There will likely be between one and two vortices in the illuminated area at a given instant. The projected tip vortex spacing of 5 m at SWiFT was estimated using the free-wake vortex method WindDVE [56] on a representative wind turbine operating at a tip-speed ratio of approximately 7. At these scales a 256 × 256 pixel velocity image corresponds to a measurement resolution on the order of 0.05 m when accounting for perspective distortion. To give that resolution a frame of reference, a continuous wave lidar system would have an approximate spatial resolution of 5 m at that working distance [11].

The proposed geometry is similar to the Sprung setup except that the scattering has shifted to a more backscatter direction. Loss of signal due to the increased receiver field of view and range are compensated for by increased laser power (assumed to be 400 mJ/pulse - the maximum for our existing laser) and lower f-number receiver optics (f/2 vs f/4 during Sprung testing). Due to the observation vectors, the velocity measurements will be primarily weighted toward the vertical velocity component. The configuration will be less sensitive to both out of plane (normal to the sheet) and horizontal velocity component measurements. Without raising the cameras higher than ground level, it will not be possible to measure both horizontal and vertical velocity components with equal sensitivity, providing the light sheet is oriented vertically. Adding a fourth receiver would also improve upon this issue by measuring an additional velocity component that can be incorporated when transforming the velocity components to a standard orthogonal coordinate system.

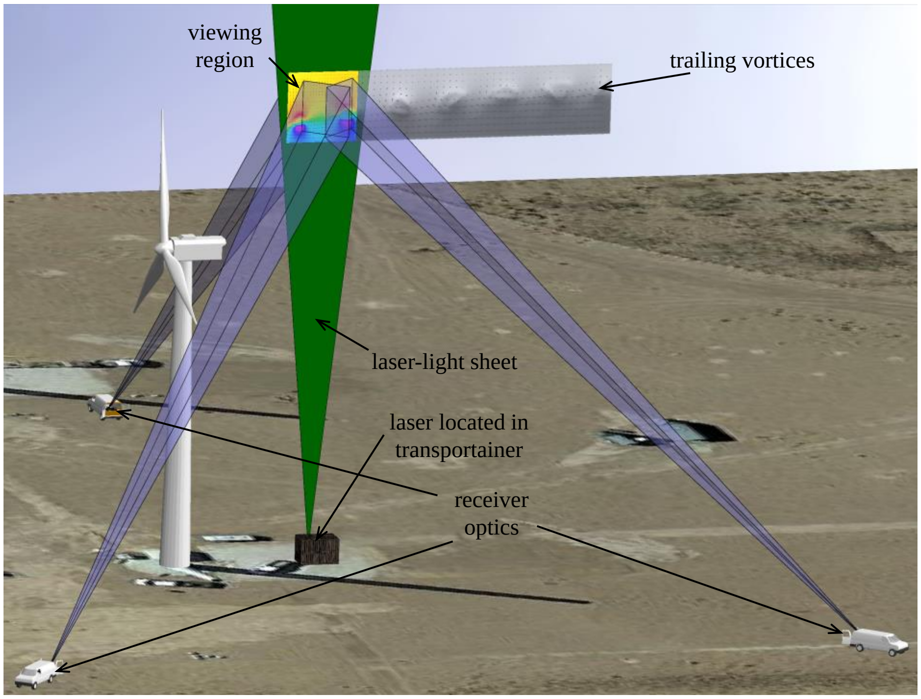

Figure 20. Schematic of the Sandia Wake Imaging System implemented at SWiFT

Figure 21 shows the noise equivalent velocity during a single shot measurement for the proposed test arrangement, assuming a differential scattering cross-section of 3.2×10^{-10} cm^2/sr, beam splitter ratio of 50/50, and laser pulse energy of 1 Joule. The calculation demonstrates that for the proposed Sandia Wake Imaging System, assuming an aerosol type and maximum concentration achieved during Sprung testing, the signal level is sufficient to obtain a single-shot, noise equivalent velocity of approximately 1 m/s at a particle concentration of about 2000 cm^{-3}. Significant work is still required in creating an outdoor aerosol generating system to reach the necessary concentrations throughout the imaging area. APS measurements at the SWiFT facility indicate that the natural aerosols follow a diurnal pattern with a concentration from as little as approximately 200 cm^{-3} to as much as 1400 cm^{-3}. As is expected, the higher observable concentrations are also associated with a larger fraction of particles sized larger than 1 μm.

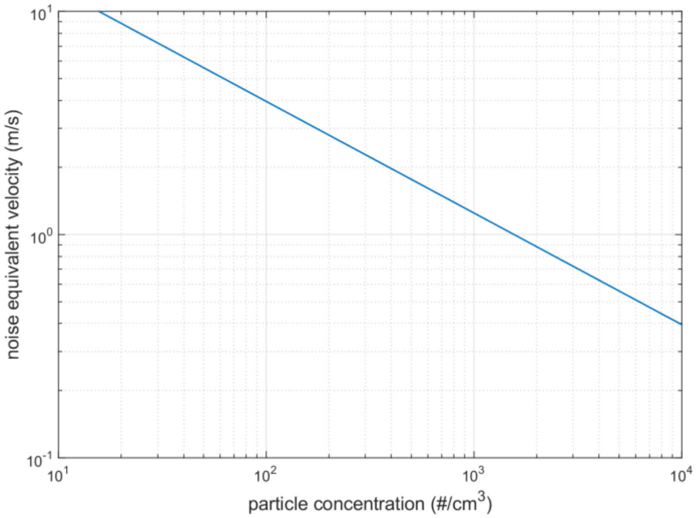

Figure 21. Noise equivalent velocity vs particle concentration for proposed SWiFT setup of the Sandia Wake Imaging System.

Alternative arrangements and variations are also being considered. These include: 1) raising the receivers to a higher level thereby decreasing range (and improving the sensitivity to the horizontal component of the wind velocity), 2) measuring the vortices at the lowest point of the rotor (near-wall shear layer of the wake), 3) measuring the vortices through a perpendicular plane along the side shear layer of the wake, and 4) increasing the receiver field of view. Trade studies must be conducted, with representation from the concurrent modeling efforts, to determine the most useful configuration(s).

VII. Conclusions

Recently, new velocity measurement technologies have been successfully implemented on large scales to better understand the flow field within wind farms and in the vicinity of wind turbines. However, a velocity measurement tool that captures the instantaneous coherent structures of the incoming atmosphere and wind turbine flow field at sufficient resolution for validation of high-fidelity modeling codes does not currently exist. To address this measurement gap, Sandia National Laboratories began developing the Sandia Wake Imaging System (SWIS) in 2012. SWIS uses the Doppler Global Velocimetry (DGV) technique to acquire instantaneous velocity images within a laser sheet projected over a large field of view. DGV was chosen due to its ability to capture instantaneous velocity fields with improved scaling capabilities compared to other velocity diagnostics. The current work demonstrated a scaled outdoor demonstration to bridge the technology development between previously conducted laboratory tests and the planned field tests to be conducted at the Scaled Wind Farm Technology (SWiFT) facility. A successful single-component velocity measurement over a 2 m × 2 m viewing area of a representative 16.5 m/s flowfield generated by a 1 m diameter industrial fan was demonstrated. The average velocity measurement was compared to an independent sonic anemometer measurement with strong agreement. Instantaneous velocity measurements were acquired with a noise level ranging from ±1.8 m/s to ±3.3 m/s depending on the generated aerosol concentration. The system sensitivity limits were analyzed by varying the aerosol concentration in a zero-velocity flowfield and measuring the corresponding signal levels on the receiver. An uncertainty analysis of the noise sources within the system revealed that the performance of the imaging system is most likely limited by shot noise of the signal photons. This analysis also discovered that the shot noise between the signal and reference camera was in all likelihood correlated and that changing the beam splitter ratio of the signal/reference camera from 50/50 to 65/35 may minimize the noise equivalent velocity of the measurement. The system sensitivity limits were used to calibrate radiometric modeling used to scale the system for deployment at the SWiFT facility. The radiometric model indicates that a ±1 m/s velocity noise is feasibly possible on a 5 m × 5 m viewing region (approximate distance between tip vortices at SWiFT) using a similar (somewhat more powerful) laser to the present experiment, larger aperture lenses on the receiver, and additional aerosol generation augmenting the naturally occurring aerosols. Based upon the results of the current intermediate-scale field tests, the specifications and capabilities of SWIS have been defined with significantly higher confidence.

Acknowledgments

This work was funded by the US Department of Energy Wind and Water Power Technologies Office. In addition to our DOE sponsors, the authors would like to acknowledge our fellow Sandia National Laboratories colleagues Mark Johnson and Alice Sobczak for their ongoing technical contributions to the project. Additionally, we thank Carsten Westergaard of NextraTEC and James Meyers of NASA Langley Research Center for providing expert technical advice, historical perspective, and extensive technical discussions that have significantly benefited the project.

References

1. Barthelmie, R. J., Hansen, K., Frandsen, S. T., Rathmann, O., Schepers, J. G., Schlez, W., Phillips, J., Rados, K., Zervos, A., Politis, E. S., and Chaviaropoulos, P. K. "Modelling and measuring flow and wind turbine wakes in large wind farms offshore," *Wind Energy* Vol. 12, No. 5, 2009, pp. 431-444.
2. Barthelmie, R. J., Frandsen, S. T., Nielsen, M. N., Pryor, S. C., Rethore, P. E., and Jørgensen, H. E. "Modelling and measurements of power losses and turbulence intensity in wind turbine wakes at Middelgrunden offshore wind farm," *Wind Energy* Vol. 10, No. 6, 2007, pp. 517-528.
3. Sherry, M., Nemes, A., Lo Jacono, D., Blackburn, H. M., and Sheridan, J. "The interaction of helical tip and root vortices in a wind turbine wake," *Physics of Fluids* Vol. 25, No. 11, 2013.
4. Hirth, B. D., Schroeder, J. L., Gunter, W. S., and Guynes, J. G. "Coupling Doppler radar-derived wind maps with operational turbine data to document wind farm complex flows," *Wind Energy*, 2014.
5. Barthelmie, R. J., Pryor, S. C., Frandsen, S. T., Hansen, K. S., Schepers, J. G., Rados, K., Schlez, W., Neubert, A., Jensen, L. E., and Neckelmann, S. "Quantifying the Impact of Wind Turbine Wakes on Power Output at Offshore Wind Farms," *Journal of Atmospheric and Oceanic Technology* Vol. 27, No. 8, 2010, pp. 1302-1317.
6. Barthelmie, R. J., and Jensen, L. E. "Evaluation of wind farm efficiency and wind turbine wakes at the Nysted offshore wind farm," *Wind Energy* Vol. 13, No. 6, 2010, pp. 573-586.
7. McKay, P., Carriveau, R., and Ting, D. S. K. "Wake impacts on downstream wind turbine performance and yaw alignment," *Wind Energy* Vol. 16, No. 2, 2013, pp. 221-234.
8. Hansen, K. S., Barthelmie, R. J., Jensen, L. E., and Sommer, A. "The impact of turbulence intensity and atmospheric stability on power deficits due to wind turbine wakes at Horns Rev wind farm," *Wind Energy* Vol. 15, No. 1, 2012, pp. 183-196.
9. Hong, J., Toloui, M., Chamorro, L. P., Guala, M., Howard, K., Riley, S., Tucker, J., and Sotiropoulos, F. "Natural snowfall reveals large-scale flow structures in the wake of a 2.5-MW wind turbine," *Nature Communications* Vol. 5, 2014.
10. Naughton, J. "Instrumentation and Test Facility Needs for Wind Turbine Technology Development," *50th AIAA Aerospace Sciences Meeting including the New Horizons Forum and Aerospace Exposition*. American Institute of Aeronautics and Astronautics, 2012.
11. Sjöholm, M., Angelou, N., Hansen, P., Hansen, K. H., Mikkelsen, T., Haga, S., Silgjerd, J. A., and Starsmore, N. "Two-Dimensional Rotorcraft Downwash Flow Field Measurements by Lidar-Based Wind Scanners with Agile Beam Steering," *Journal of Atmospheric and Oceanic Technology* Vol. 31, No. 4, 2013, pp. 930-937.
12. Bingöl, F., Mann, J., and Larsen, G. C. "Light detection and ranging measurements of wake dynamics part I: one-dimensional scanning," *Wind Energy* Vol. 13, No. 1, 2010, pp. 51-61.
13. Trujillo, J.-J., Bingöl, F., Larsen, G. C., Mann, J., and Kühn, M. "Light detection and ranging measurements of wake dynamics. Part II: two-dimensional scanning," *Wind Energy* Vol. 14, No. 1, 2011, pp. 61-75.
14. Iungo, G. V., and Porté-Agel, F. "Volumetric scans of wind turbine wakes performed with three simultaneous wind LiDARs under different atmospheric stability regimes," *Journal of Physics: Conference Series* Vol. 524, No. 1, 2014.
15. Hirth, B. D., and Schroeder, J. L. "Documenting Wind Speed and Power Deficits behind a Utility-Scale Wind Turbine," *Journal of Applied Meteorology and Climatology* Vol. 52, No. 1, 2012, pp. 39-46.
16. Hirth, B. D., Schroeder, J. L., Gunter, W. S., and Guynes, J. G. "Measuring a Utility-Scale Turbine Wake Using the TTUKa Mobile Research Radars," *Journal of Atmospheric and Oceanic Technology* Vol. 29, No. 6, 2012, pp. 765-771.
17. Toloui, M., Riley, S., Hong, J., Howard, K., Chamorro, L. P., Guala, M., and Tucker, J. "Measurement of atmospheric boundary layer based on super-large-scale particle image velocimetry using natural snowfall," *Experiments in Fluids* Vol. 55, No. 5, 2014, pp. 1-14.
18. Morris, S. C., Stolpa, S. R., Slaboch, P. E., and Klewicki, J. C. "Near-surface particle image velocimetry measurements in a transitionally rough-wall atmospheric boundary layer," *Journal of Fluid Mechanics* Vol. 580, 2007, pp. 319-338.
19. Adrian, R. J., and Westerweel, J. *Particle Image Velocimetry*: Cambridge University Press, 2011.
20. Scarano, F., and Westerweel, J. "Particle Image Velocimetry," *Springer Handbook of Experimental Fluid Mechanics*. Springer, 2007, pp. 309-342.
21. Pol, S. U., and Balakumar, B. J. "Design considerations for large field particle image velocimetery (LF-PIV)," *Measurement Science and Technology* Vol. 24, No. 2, 2013.
22. Bosbach, J., Kühn, M., and Wagner, C. "Large scale particle image velocimetry with helium filled soap bubbles," *Experiments in Fluids* Vol. 46, No. 3, 2009, pp. 539-547.

23. Scarano, F., Ghaemi, S., Caridi, G., Bosbach, J., Dierksheide, U., and Sciacchitano, A. "On the use of helium-filled soap bubbles for large-scale Tomographic PIV wind tunnel experiments," *13th International Symposium on Applications of Laser Techniques to Fluid Mechanics*. Lisbon, Portugal, 2014.
24. Meyers, J. F., Lee, J. W., and Cavone, A. A. "Doppler Global Velocimetry," *Springer Handbook of Experimental Fluid Mechanics*. Springer, 2007, pp. 342-353.
25. Meyers, J. F., Lee, J. W., and Schwartz, R. J. "Characterization of measurement error sources in Doppler global velocimetry," *Measurement Science and Technology* Vol. 12, 2001, pp. 357-368.
26. McKenzie, R. L. "Measurement capabilities of planar Doppler velocimetry using pulsed lasers," *Applied Optics* Vol. 35, No. 6, 1996, pp. 948-964.
27. Berg, J., Bryant, J., LeBlanc, B., Maniaci, D. C., Naughton, B., Paquette, J. A., Resor, B. R., White, J., and Kroeker, D. "Scaled Wind Farm Technology Facility Overview," *32nd ASME Wind Energy Symposium*. American Institute of Aeronautics and Astronautics, 2014.
28. Mikkelsen, T. "Lidar-based Research and Innovation at DTU Wind Energy – a Review," *Journal of Physics: Conference Series* Vol. 524, No. 1, 2014.
29. Mikkelsen, T., Mann, J., Courtney, M., and Sjöholm, M. "Windscanner: 3-D wind and turbulence measurements from three steerable doppler lidars," *IOP Conference Series: Earth and Environmental Science*, 2008.
30. Mosedale, A. D., Elliott, G. S., Carter, C. D., and Beutner, T. J. "Planar Doppler Velocimetry in a Large-Scale Facility," *AIAA Journal* Vol. 38, No. 6, 2000, pp. 1010-1024.
31. Elliott, G. S., and Beutner, T. J. "Molecular filter based planar Doppler velocimetry," *Progress in Aerospace Sciences* Vol. 35, No. 8, 1999, pp. 799-845.
32. Elliott, G. S., Crafton, J., Baust, H. D., Beutner, T. J., Carter, C. D., and Tyler, C. "Evaluation and Optimization of a Multi-component Planar Doppler Velocimetry System," *43rd AIAA Aerospace Sciences Metting*. Reno Nevada, 2005.
33. McKenzie, R. L., and Reinath, M. S. "Three Dimensional Planar Doppler Velocity Measurements in a Full-Scale Rotor Wake," *AIAA Journal* Vol. 43, No. 3, 2005, pp. 489-499.
34. Charrett, T. O. H., Nobes, D. S., and Tatam, R. P. "Investigation into the selection of viewing configurations for three-component planar Doppler velocimetry measurements," *Applied Optics* Vol. 46, No. 19, 2007, pp. 4102-4116.
35. Morrison, G. L., and Gaharan, C. A. J. "Uncertainty estimates in DGV systems due to pixel location and velocity gradients," *Measurement Science and Technology* Vol. 12, No. 4, 2001, p. 369.
36. Nobes, D. S., Wieneke, B., and Tatam, R. P. "Determination of view vectors from image warping mapping functions," *Optical Engineering* Vol. 43, No. 2, 2004, pp. 407-414.
37. Willert, C. E. "Assessment of camera models for use in planar velocimetry calibration," *Experiments in Fluids* Vol. 41, No. 1, 2006, pp. 135-143.
38. Bohren, C. F., and Huffman, D. R. *Absorption and Scattering of Light by Small Particles*: John Wiley & Sons, Inc., 1983.
39. Mätzler, C. "MATLAB Functions for Mie Scattering and Absorption." Research Report No. 2002-08 Institute of Applied Physics, University of Bern, 2002.
40. Williams, T. C., and Shaddix, C. R. "Simultaneous correction of flat field and nonlinearity response of intensified charge-coupled devices," *Review of Scientific Instruments* Vol. 78, No. 12, 2007.
41. Lee, J., and Meyers, J. "Increase Accuracy in Molecular Filter Based Flow Field Diagnostics Through Direct Frequency Calibration Using Optical Modulators," *43rd AIAA Aerospace Sciences Meeting and Exhibit*. American Institute of Aeronautics and Astronautics, 2005.
42. Forkey, J. N., Lempert, W. R., and Miles, R. B. "Corrected and calibrated I2 absorption model at frequency-doubled Nd:YAG laser wavelengths," *Applied Optics* Vol. 36, No. 27, 1997, pp. 6729-6738.
43. Forkey, J. N., Lempert, W. R., and Miles, R. B. "Observation of a 100-MHz frequency variation across the output of a frequency-doubled injection-seeded unstable-resonator Q-switched Nd:YAG laser," *Optics Letters* Vol. 22, No. 4, 1997, pp. 230-232.
44. Morrison, G. L., and Suryanarayanan, S. "DGV's Accuracy Dependence Upon Laser Beam Intensity Profile," *ASME 2009 Fluids Engineering Division Summer Meeting*. FEDSM2009-78245, 2009.
45. Fischer, M., Heinze, J., Matthias, K., and Röhle, I. "Doppler Global Velocimetry in flames using a newly developed, frequency stabilized, tunable, long pulse Nd:YAG laser," *10th International Symposium on Applications of Laser Techniques to Fluid Mechanics*. Lisbon, Portugal, 2000.
46. Fischer, M., Stockhausen, G., Heinze, J., Seifert, M., Müller, R., and Schodl, R. "Development of DopplerGlobal Velocimetry (DGV) measurement devices and combined application of DGV and OH*-chemiluminescence imaging to gas turbine combustor," *12th International Symposium on Applications of Laser Techniques to Fluid Mechanics*. Lisbon, Portugal, 2004.
47. Schodl, R., Röhle, I., Willert, C., Fischer, M., Heinze, J., Laible, C., and Schilling, T. "Doppler global velocimetry for the analysis of combustor flows," *Aerospace Science and Technology* Vol. 6, No. 7, 2002, pp. 481-493.
48. Willert, C., Hassa, C., Stockhausen, G., Jarius, M., Voges, M., and Klinner, J. "Combined PIV and DGV applied to a pressurized gas turbine combustion facility," *Measurement Science and Technology* Vol. 17, No. 7, 2006.
49. Smith, M. "The reduction of laser speckle noise in planar Doppler velocimetry systems," *20th AIAA Advanced Measurement and Ground Testing Technology Conference*. American Institute of Aeronautics and Astronautics, 1998.
50. Fischer, A., König, J., and Czarske, J. "Speckle noise influence on measuring turbulence spectra using time-resolved Doppler global velocimetry with laser frequency modulation," *Measurement Science and Technology* Vol. 19, No. 12, 2008.

51. Fischer, A., Büttner, L., Czarske, J., Eggert, M., and Müller, H. "Measurement uncertainty and temporal resolution of Doppler global velocimetry using laser frequency modulation," *Applied Optics* Vol. 47, No. 21, 2008, pp. 3941-3953.
52. Fischer, A., Büttner, L., Czarske, J., Eggert, M., and Müller, H. "Measurements of velocity spectra using time-resolving Doppler global velocimetry with laser frequency modulation and a detector array," *Experiments in Fluids* Vol. 47, No. 4-5, 2009, pp. 599-611.
53. Fischer, A., Pfister, T., and Czarske, J. "Derivation and comparison of fundamental uncertainty limits for laser-two-focus velocimetry, laser Doppler anemometry and Doppler global velocimetry," *Measurement* Vol. 43, No. 10, 2010, pp. 1556-1574.
54. Fischer, A., Haufe, D., Büttner, L., and Czarske, J. "Scattering effects at near-wall flow measurements using Doppler global velocimetry," *Applied Optics* Vol. 50, No. 21, 2011, pp. 4068-4082.
55. Wang, H., Gao, Q., and JinJun, W. "Proper orthogonal decomposition based outlier correction for PIV data," *17th international Symposium on Applications of laser Techniques to Fluid Mechanics*. Lisbon, Portugal, 2014.
56. Maniaci, D. "Wind Turbine Design Using A Free-wake Vortex Method with Winglet Application," *Aerospace Engineering*. Ph.D., Pennsylvania State University, 2013.